Atmos. Meas. Tech. Discuss., 6, 8889–8935, 2013
www.atmos-meas-tech-discuss.net/6/8889/2013/
doi:10.5194/amtd-6-8889-2013

Atmospheric Measurement Techniques Discussions

Vertical profile of δ^{18}OOO from middle stratosphere to lower mesosphere derived by retrieval algorithm developed for SMILES spectra

T. O. Sato[1,2], **H. Sagawa**[2], **N. Yoshida**[1,3], **and Y. Kasai**[2,1]

[1]Tokyo Institute of Technology, 4259 Nagatsuta, Midori, Yokohama, Kanagawa 226-8503, Japan
[2]National Institute of Information and Communications Technology, 4-2-1 Nukui-kitamachi, Koganei, Tokyo 184-8795, Japan
[3]Earth-Life Science Institute, 2-12-1 Ookayama, Meguro, Tokyo 152-8551, Japan

Received: 22 August 2013 – Accepted: 26 September 2013 – Published: 15 October 2013

Correspondence to: T. O. Sato (sato.t.ak@m.titech.ac.jp)

Published by Copernicus Publications on behalf of the European Geosciences Union.

Abstract

Ozone is known to have large oxygen isotopic enrichments of about 10 % in the middle stratosphere, however, there have been no reports on ozone isotopic enrichments above the middle stratosphere. We derived an enrichment δ^{18}OOO by a retrieval algorithm specified for the isotopic ratio from the stratosphere to the lower mesosphere based on observations from the Superconducting Submillimeter-Wave Limb–Emission Sounder (SMILES) onboard the International Space Station (ISS). The retrieval algorithm includes (i) an a priori covariance matrix constrained by oxygen isotopic ratios in ozone, (ii) an optimization of spectral windows for ozone isotopomers and isotopologues, and (iii) a common tangent height information for all windows. The δ^{18}OOO obtained by averaging the SMILES measurements at the latitude range of 20° N to 40° N from February to March in 2010 with solar zenith angle < 80° was 15 % (at 32 km) and the systematic error was estimated to be about 5 %. SMILES and past measurements were in good agreement with δ^{18}OOO increasing with altitude between 30 and 40 km. The vertical profile of δ^{18}OOO obtained in this study showed an increase and a decrease with altitude in the stratosphere and mesosphere, respectively. Stratopause is the peak-height of the δ^{18}OOO value, and it rose to 18 %. The δ^{18}OOO has a positive correlation with temperature in the range of 220–255 K, indicating that temperature can be a dominant factor to control the vertical profile of δ^{18}OOO in the stratosphere and mesosphere. This is the first report of the observation of δ^{18}OOO over a wide range extending from the stratosphere to the mesosphere.

1 Introduction

Ozone plays an important role in the Earth's atmosphere, and its pronounced oxygen isotopic signature affects a host of an oxygen isotopic ratio in other trace constituents

AMTD
6, 8889–8935, 2013

such as CO_2 and N_2O (Lyons, 2001). Isotopic enrichment is defined as

$$\delta^{m}O = \frac{{}^{m}R_{obs}}{{}^{m}R_{std}} - 1, {}^{m}R = \frac{[{}^{m}O]}{[{}^{16}O]}, (m = 17, 18). \quad (1)$$

In this paper, the oxygen isotopic ratio of standard mean ocean water (SMOW) is used as the standard R_{std} (SMOW: $^{16}O : {}^{17}O : {}^{18}O = 1 : 1/2700 : 1/500$).

Observation of oxygen isotopic enrichments in ozone was started by balloon-based in-situ experiments using a mass spectrometer (Mauersberger, 1981). The observed $\delta^{18}O$ in bulk ozone was increased from 7 % to 12 % at 21 and 34 km, respectively (Krankowsky et al., 2007). This trend is relatively consistent with the temperature dependence of $\delta^{18}O$ generated by the ozone formation reaction:

$$O + O_2 + M \rightarrow O_3 + M, \quad (R1)$$

where $\delta^{18}O$ increases with temperature (e.g., Morton et al., 1990; Hathorn and Marcus, 1999; Gao and Marcus, 2001). A latitudinal variation of $\delta^{18}O$ which was more pronounced near the equator than at the middle latitude regions was reported, although the observations had been performed in different years (Krankowsky et al., 2007).

Measurement using a mass spectrometer has an advantage of high accuracy (0.01–0.1 %), but it is hard to distinguish molecules that have same mass with different isotopomers such as ^{18}OOO (asymmetric-18 ozone) and $O^{18}OO$ (symmetric-18 ozone). Using spectroscopic measurement technique asymmetric and symmetric isotopomers are separately observed. Irion et al. (1996) observed oxygen isotopic enrichments in middle stratospheric ^{18}OOO and $O^{18}OO$ using space-based solar occultation spectra by the Atmospheric Trace Molecule Spectroscopy (ATMOS). Their globally averaged enrichments between 24 and 41 km were 15 ± 6 % and 10 ± 7 % for ^{18}OOO and $O^{18}OO$, respectively. They showed that ^{18}OOO was more enriched than $O^{18}OO$, which was supported by the measurements using a balloon- and aircraft-based Fourier transform infrared (FTIR) spectrometer by Johnson et al. (2000) and Haverd et al. (2005).

AMTD
6, 8889–8935, 2013

The ozone formation reaction (R1) is a primary source of oxygen isotopic enrichments in ozone, and there is another contribution from photolysis:

$$O_3 + h\nu \rightarrow O + O_2, \quad \text{(R2)}$$

especially above 30 km. Liang et al. (2006) separately calculated the vertical profiles of ozone isotopic enrichments due to the formation process and photolysis using the 1–D Caltech/JPL KINETICS model. The maximum ^{18}OOO produced by photolysis was 3 % at 35 km. Haverd et al. (2005) observed the vertical profiles of δ^{18}OOO and δO^{18}OO using balloon-based solar remote sensing FTIR absorption spectroscopy. They showed significant increases with altitude of these photolytic fractionation profiles (δ^{18}OOO = 4 % at 35 km) and the importance of photochemistry for the ozone isotopic composition.

The Superconducting Submillimeter-Wave Limb-Emission Sounder (SMILES) is an instrument to observe atmospheric submillimeter-wave emission using superconducting technology for radiation-receiving systems (Kikuchi et al., 2010). It provides quite low-noise spectra and makes observations at higher altitudes (lower densities) possible. The signal-to-noise ratios of the ^{18}OOO transition at 649.137 GHz are about 40 and 3 in the stratosphere and mesosphere, respectively, for a single-scan observation. Vertical profile of O_3 concentration was observed up to the upper mesosphere using SMILES observation data (Kasai et al., 2013). SMILES was launched and docked on the Japanese Experiment Module (JEM) of the International Space Station (ISS) in September 2009. The operation period was between 12 October 2009 and 21 April 2010. SMILES is equipped with two acousto optical spectrometers (AOSs), named AOS 1 and AOS 2, with a bandwidth of 1.2 GHz and has three observation frequency bands in the submillimeter-wave region (Band A: 624.32–625.52 GHz, Band B: 625.12–626.32 GHz, Band C: 649.12–650.32 GHz), i.e., two bands are simultaneously observed. The transitions of O_3, ^{18}OOO, O^{18}OO, ^{17}OOO and O^{17}OO are located in the SMILES bands although the intensity of the transition of O^{18}OO is quite small (see Fig. 1). Prior to the SMILES launch, Kasai et al. (2006) estimated the expected precision and accuracy of SMILES ozone isotopic enrichment observations. They re-

AMTD
6, 8889–8935, 2013

ported a precision of a few percent over a 10° daily zonal mean profile and an accuracy of about 15 % for the enrichments for ^{18}OOO, ^{17}OOO and O^{17}OO. There have been many improvements in the SMILES observation such as a spectrum non-linear gain calibration, retrieval algorithm and model parameters since the launch. SMILES has a possibility to observe ozone isotopic enrichments above the middle stratosphere.

In this study, we developed a retrieval algorithm optimized for ozone isotopic enrichments using SMILES observation data. Section 2 describes the details of the specified retrieval algorithm. In Sect. 3, the error in δ^{18}OOO derived from the specified retrieval algorithm is estimated by a quantitative error analysis, and the averaged δ^{18}OOO values in a latitude range of 20° N to 40° N from February to March in 2010 in the daytime (solar zenith angle < 80°) were compared with past measurements. The δ^{18}OOO in the altitude region from the upper stratosphere to the lower mesosphere is discussed in Sect. 4. We report, for the first time, vertical profile observations of δ^{18}OOO encompassing both the stratosphere and the mesosphere.

2 Development of retrieval algorithm

We developed the optimized retrieval algorithm for ozone isotopic ratio by SMILES (TOROROS). This algorithm is based on the SMILES NICT Level 2 retrieval algorithm version 2.1.5 (called "V215" in this paper). The SMILES retrieval algorithm is based on the least-squares method with an a priori constraint (e.g., Rodgers, 2000). The forward model consists of a clear-sky radiative transfer model and the numerical instrument functions of SMILES. A detailed description for the version 2.X.X series of the SMILES NICT Level 2 processing, including V215, can be found in Baron et al. (2011).

2.1 Level-1b spectrum and tangent height correction

We employed the Level-1b (L1b) data version 008 released in 2012. This version updated a non-linear gain calibration of spectrum brightness temperature (Ochiai et al.,

AMTD
6, 8889–8935, 2013

2012a). As emphasized by Kasai et al. (2013), the non-linearity issue was one of the biggest causes of error in the retrieval of the O_3 VMR in the V215 processing. The tangent height information was also improved using data acquired by the SMILES star tracker sensor and the Monitor of All-sky X-ray Image (MAXI) (Ochiai et al., 2012b).

We used the tangent height after correcting it by a bias offset in TOROROS. The bias offset was estimated by comparing the brightness temperatures observed by SMILES with those calculated by the forward model in the frequency range of 649.56 to 649.69 GHz. The intensities of transitions in this frequency range are quite small, therefore, the effect from atmospheric molecular radiations and their variations are minimized. The method of this bias estimation was not changed from V215 (see Sect. 3 of Baron et al., 2011, for detail). The forward model is described in Sect. 2.3. The bias offset was estimated to be about 2–3 km. The corrected tangent height was directly introduced to retrievals of volume mixing ratio (VMR) in the following spectral windows with limited frequency ranges.

2.2 Window configuration

As mentioned in Sect. 1, two of the three bands are simultaneously observed. The AOSs assigned to Bands B and C are fixed, i.e., the observations of Bands B and C are always performed by AOS 2 and AOS 1, respectively. We used only data of the observation for Bands B and C for this study so as not to cause any undesirable errors due to observation differences with the band configuration. Band A is flexibly observed by AOS 1 and AOS 2 depending on the other band that is observed with Band A. The O_3 VMR is preferably retrieved from Band B rather than Band A in this study.

We set three spectral windows to retrieve the VMR of O_3 and ^{18}OOO in Bands B and C, and one spectral window for the temperature (see Fig. 1 and Table 1). Setting windows with a small frequency range has the advantage of reducing contaminations from transitions of molecules different from the target. The retrieval processes of the four windows were independent of each other to prevent any error propagation from

AMTD
6, 8889–8935, 2013

window to window and to avoid retrieving the VMRs of O_3 and ^{18}OOO with different weights due to the difference of their spectral line intensities.

Window b1 in Band B was set to retrieve the VMR of O_3 using the transition at 625.371 GHz. The frequency range was between 625.042 and 625.642 GHz. Other parameters were simultaneously retrieved; the VMRs of other molecules (^{18}OOO, ozone in the vibrational state O_3^*, H_2O, HNO_3 and HOCl), the frequency shift and the spectrum baseline of the first-order polynomial function. The pressure and temperature profile was fixed to be the a priori (described in Sect. 2.4). The intervals of the retrieval altitude grid were 4 and 5 km at altitudes below and above 30 km, respectively. This altitude grid was commonly applied for the other windows.

Two windows were set in Bands B and C for ^{18}OOO. Window b2 in Band B retrieves the ^{18}OOO VMR using the transition at 625.564 GHz that is located at the wing of the O_3 line at 625.371 GHz. The VMR of O_3 was simultaneously retrieved to fit a spectrum baseline. Window c1 in Band C retrieves the VMR of ^{18}OOO using the lines at 649.137 and 649.152 GHz. The VMR of ^{17}OOO is also retrieved with the transition at 649.275 GHz in window c1. These transitions are isolated from other strong lines. Frequency shifts and second-order polynomial functions were also retrieved for spectrum baseline corrections in both b2 and c1.

In window b0, the temperature was retrieved from the O_3 line at 625.371 GHz. The frequency range and the retrieved parameters were the same as window b1.

There are $O^{18}OO$ transitions at 624.505 and 624.825 GHz in Band A, but unfortunately their intensities are too weak to retrieve the VMR of $O^{18}OO$ for the purpose of a discussion on the isotopic ratio. Moreover, the transitions of CH_3CN, which are located quite close to the $O^{18}OO$ transitions, cause large contaminations. In this paper a retrieval of the $O^{18}OO$ VMR is not discussed.

AMTD
6, 8889–8935, 2013

2.3 Forward model

We employed the forward model ($\mathcal{F}$) in V215 with the following improvements. Spectroscopic parameters were one of the largest error sources in the retrieval of the VMR of O_3 for V215 (Kasai et al., 2013), and those of the ozone isotopomers and isotopologues were updated based on the JPL catalog (Pickett et al., 1998), the HITRAN 2008 database (Rothman et al., 2009), and the latest laboratory experiments (e.g., Drouin and Gamache, 2008). Table 2 summarizes the spectroscopic parameters of the ozone isotopomers and isotopologues used in windows b1, b2, and c1.

Instrument functions have been improved from those in V215 with respect to an antenna beam pattern (R_{ANT}), a sideband separator (SBS) and an AOS response function. R_{ANT} was implemented with a two-step modification. First, R_{ANT} was integrated in the vertical direction considering the SMILES field-of-view. The atmosphere is assumed to be horizontally stratified and only the integration in the vertical direction was performed. Second, R_{ANT} was widened taking into account the accumulation of atmospheric limb emissions over 0.5 s (six steps of the antenna moving with a stepping rate of 12 Hz) to generate a spectrum at one tangent height. A rejection rate of the image band (β_{image}) was implemented considering the SBS characteristics. We employed the AOS response function improved by Mizobuchi et al. (2012). It is contained in the L1b data version 008. The AOS response function was obtained by fitting with three Gaussian components. The accuracy of the fitting is better than that in the L1b data version 007. The error in the AOS response function used in TORORO was estimated to be about 5 % in full width at half maximum (FWHM), which was half that of the previous version (10 %).

AMTD
6, 8889–8935, 2013

2.4 Inversion calculation

In the TOROROS algorithm, a solution of the retrieval state vector $\boldsymbol{x}$ is determined by minimizing the following cost function χ^2:

$$\chi^2 = \frac{(\boldsymbol{y} - \mathcal{F}(\boldsymbol{x}, \boldsymbol{b}))^{\mathrm{T}} \mathbf{S}_y{}^{-1} (\boldsymbol{y} - \mathcal{F}(\boldsymbol{x}, \boldsymbol{b}))}{n_y} + \frac{(\boldsymbol{x} - \boldsymbol{x}_{\mathrm{a}})^{\mathrm{T}} \mathbf{S}_x{}^{-1} (\boldsymbol{x} - \boldsymbol{x}_{\mathrm{a}})}{n_x}. \quad (2)$$

This definition of χ^2 is slightly different from that in V215 (see Eq. (2) in Baron et al., 2011) to increase the contribution of the a priori constraint. $\boldsymbol{y}$ is the vector of the observed spectrum, $\boldsymbol{b}$ is the model parameter vector, and n_x and n_y are the numbers of elements of $\boldsymbol{x}$ and $\boldsymbol{y}$, respectively. $\mathbf{S}_y$ and $\mathbf{S}_x$ are covariance matrices for the measurement spectrum noise and an a priori state ($\boldsymbol{x}_{\mathbf{a}}$), respectively. $\mathbf{S}_y$ is the diagonal matrix with the diagonal elements of $(0.5\mathrm{K})^2$. $\boldsymbol{x}_{\mathrm{a}}$ of the O_3 VMR was the same as V215 and was taken from the Goddard Earth Observing System Model, version 5.2 (GEOS-5) (Rienecker et al., 2008) at altitudes below 60 km and the VMR value at 60 km was extended to 120 km. A priori VMR profiles of the other ozone isotopomers and isotopologues were calculated for each scan based on knowledge from past measurements of the oxygen isotopic ratio in ozone. The ^{18}OOO a priori VMR was calculated based on the O_3 a priori VMR to follow 10 % δ^{18}OOO against the SMOW standard for all altitudes. The O^{18}OO a priori VMR was 5 % δO^{18}OO following a statistical rule. The a priori VMRs of ^{17}OOO and O^{17}OO were calculated using the relationship of mass-dependent fractionation ($\delta^{17}\mathrm{O} = 0.515\delta^{18}\mathrm{O}$).

The a priori profiles of pressure and temperature were taken from GEOS-5 and the Mass Spectrometer and Incoherent Scatter (MSIS) climatology (Hedin, 1991), as implemented in V215. The former was for the altitude region from the surface to 70 km

AMTD
6, 8889–8935, 2013

and the latter was from 70 to 120 km. They were smoothly interpolated assuming a hydrostatic equilibrium.

We implemented cross terms between the ozone isotopomers and isotopologues in $\mathbf{S}_x$ following the retrieval of the HDO/H_2O ratio from the Tropospheric Emission Spectrometer (TES) observation (Worden et al., 2006). It is expected to prevent the estimated isotopic ratio to be unrealistic value and reduce its dispersion.

The retrieval parameter was projected from the linear scale to the log scale ($\boldsymbol{x} \rightarrow \boldsymbol{z}$).

$$\boldsymbol{z} = \ln(\boldsymbol{x}) \tag{3}$$

The weighting function $\mathbf{K}_x$ in the linear scale was also projected onto the log scale.

$$\mathbf{K}_z = \frac{\mathrm{d}\boldsymbol{y}}{\mathrm{d}\boldsymbol{z}} = \frac{\mathrm{d}\boldsymbol{y}}{\mathrm{d}\boldsymbol{x}}\frac{\mathrm{d}\boldsymbol{x}}{\mathrm{d}\boldsymbol{z}} = \mathbf{K}_x\boldsymbol{x} \tag{4}$$

In the case of windows b1 and b2, the VMRs of O_3 and ^{18}OOO were simultaneously retrieved. The covariance matrix for their variations in the a priori profiles was given by

$$\mathbf{S}_z = \begin{pmatrix} {}^{16,16}\mathbf{S}_z & {}^{16,16}\mathbf{S}_z \\ {}^{16,16}\mathbf{S}_z & {}^{18,18}\mathbf{S}_z \end{pmatrix}. \tag{5}$$

${}^{16,16}\mathbf{S}_z$ and ${}^{18,18}\mathbf{S}_z$ are the covariance matrices for O_3 ($^{16}\boldsymbol{z}$) and ^{18}OOO ($^{18}\boldsymbol{z}$) in the log scale, respectively. Here we assumed that the O_3 VMR was uncorrelated with the oxygen isotopic ratio (see the explanation of Eq. (21) in Worden et al., 2006).

$${}^{\mathrm{mm}}\mathbf{S}_z[i,j] = {}^{\mathrm{m}}\boldsymbol{\epsilon}_z[i]\,{}^{\mathrm{m}}\boldsymbol{\epsilon}_z[j]\exp\left[-\frac{|\boldsymbol{h}[i]-\boldsymbol{h}[j]|}{h_{\mathrm{c}}}\right], \tag{6}$$

$(\mathrm{m} = 16, 18)$

i and j in square brackets indicate the index of a matrix or a vector. $\boldsymbol{h}$ is the vector of the altitude. h_{c} is the correlation length and was set to 6 km. $\boldsymbol{\epsilon}_z$ was calculated from

AMTD
6, 8889–8935, 2013

the assumed variation in the a priori VMR ($\boldsymbol{\epsilon}_x$).

$$\boldsymbol{\epsilon}_z = \ln\left(1 + \frac{\boldsymbol{\epsilon}_x}{\boldsymbol{x}_a}\right) \tag{7}$$

$$\boldsymbol{\epsilon}_x[i] = \epsilon_1 \boldsymbol{x}_a[i] + \epsilon_2 \tag{8}$$

The conversion of Eq. (7) is recommended rather than $\boldsymbol{\epsilon}_z = \boldsymbol{\epsilon}_x / \boldsymbol{x}$ because it avoids quite large values in $\boldsymbol{\epsilon}_z$ if $\boldsymbol{x}_a$ includes a small VMR value (for example an order of pptv). ϵ_1 and ϵ_2 for O_3 were 0.25 and 1.0×10^{-6}, respectively. These values were conservatively estimated from the variation in the O_3 VMR (e.g., Kasai et al., 2013). The variation in δ^{18}OOO in the log scale ($^{18}\boldsymbol{\epsilon}_z$) was given by

$$^{18}\boldsymbol{\epsilon}_z[i] = \sqrt{\left(^{16}\boldsymbol{\epsilon}_z[i]\right)^2 + \left(^{R}\boldsymbol{\epsilon}_z[i]\right)^2}. \tag{9}$$

The variation of the isotopic ratio $^{R}\boldsymbol{\epsilon}_z$ was taken from the variation in the enrichment δ^{18}OOO, and $^{R}\boldsymbol{\epsilon}_z$ was set to 0.2 for all altitudes. The variations of O_3 and ^{18}OOO were multiplied by two above 55 km taking into account the accuracy of the GEOS-5 data.

In the retrieval of window c1, ^{18}OOO and ^{17}OOO were retrieved. The cross terms between the two were implemented in the same way as the retrieval of window b1 and b2, but the variation in δ^{17}OOO was assumed to be 0.3.

The retrieval state vector $\boldsymbol{z}$ was normalized with $\boldsymbol{z}_a$ ($= \ln(\boldsymbol{x}_a)$) and $\boldsymbol{\epsilon}_z$ in the retrieval iteration process.

$$\boldsymbol{\eta} = \frac{\boldsymbol{z} - \boldsymbol{z}_a}{\boldsymbol{\epsilon}_z} \tag{10}$$

AMTD
6, 8889–8935, 2013

The normalized covariance matrix ($\mathbf{S}_\eta$) was given by

$$\mathbf{S}_\eta = \begin{pmatrix} \mathbf{E} & \left({}^{18}\boldsymbol{\epsilon}_z\right)^{-1}\left({}^{16}\boldsymbol{\epsilon}_z\right)\mathbf{E} \\ \left({}^{18}\boldsymbol{\epsilon}_z\right)^{-1}\left({}^{16}\boldsymbol{\epsilon}_z\right)\mathbf{E} & \mathbf{E} \end{pmatrix}, \tag{11}$$

$$\mathbf{E}[i,j] = \exp\left[-\frac{|\boldsymbol{h}[i]-\boldsymbol{h}[j]|}{h_c}\right]. \tag{12}$$

The solution that minimizes χ^2 was determined by a Gauss–Newton iterative procedure modified by implementing the Levenverg–Marquardt scheme (Marquardt, 1963).

$$\boldsymbol{\eta}_{r+1} = \boldsymbol{\eta}_r + \left(\mathbf{K}_r^{\mathrm{T}}\mathbf{S}_y^{-1}\mathbf{K}_r + \mathbf{S}_\eta^{-1} + \Gamma\mathbf{U}\right)^{-1} \times \left(\mathbf{K}_r^{\mathrm{T}}\mathbf{S}_y^{-1}\left(\boldsymbol{y}-\mathbf{F}\left(\boldsymbol{x}_r\right)\right) - \mathbf{S}_\eta^{-1}\boldsymbol{\eta}_r\right) \tag{13}$$

Here r indicates the number of iterations. $\mathbf{K}_r$ is the weighting function at r^{th} state $\boldsymbol{\eta}_r$. The Levenberg–Marquardt parameter Γ was tuned to 2 or 1/2 and 5 or 1/5 for Band B (windows b0, b1 and b2) and Band C (window c1), respectively. $\mathbf{U}$ is the unit matrix.

3 Performance of SMILES δ^{18}OOO observation

We evaluated the δ^{18}OOO retrieved by TOROROS by 1) an error analysis and 2) a comparison study.

3.1 Error analysis

We estimated the error of the enrichment δ^{18}OOO ($\Delta\delta^{18}$OOO) by

$$\Delta\delta^{18}\mathrm{OOO} = \sqrt{\sum_{\mathrm{m}=16,18}\left[\frac{\partial\delta^{18}\mathrm{OOO}}{\partial^{\mathrm{m}}x}\cdot\Delta^{\mathrm{m}}x\right]^2}, \tag{14}$$

AMTD
6, 8889–8935, 2013

where ${}^{m}x$ and $\Delta^{m}x$ denote the VMR value and the error of O_3 (m = 16) or ${}^{18}OOO$ (m = 18), respectively. The errors $\Delta^{16}x$ and $\Delta^{18}x$ were separately calculated for each error source by error analysis with the same methodology described in Sato et al. (2012). The error sources considered in this study are summarized in Tables 3 and 4 for systematic and random errors, respectively. The total systematic and random errors were calculated by the root-sum-square of all errors caused by the considered error sources. The error in the tangent height was not included in the error analysis because its systematic error is canceled out by the tangent height bias correction described in Sect. 2.1 and Ochiai et al. (2013) estimated the precision was about 46 m which was quite smaller than the vertical resolution (about 5 km) of the VMR retrieval of O_3 and ${}^{18}OOO$.

The systematic error includes errors from the model parameters ($\Delta \boldsymbol{x}_{\text{param}}$) such as spectroscopic parameters and instrument functions. $\Delta \boldsymbol{x}_{\text{param}}$ was given by a perturbation method.

$$\Delta \boldsymbol{x}_{\text{param}} = \mathcal{J}\left(\boldsymbol{y}_{\text{ref}}, \boldsymbol{b}_0 + \Delta \boldsymbol{b}\right) - \boldsymbol{x}_{\text{ref}} \tag{15}$$
$$\boldsymbol{x}_{\text{ref}} = \mathcal{J}\left(\boldsymbol{y}_{\text{ref}}, \boldsymbol{b}_0\right), \quad \boldsymbol{y}_{\text{ref}} = \mathcal{F}\left(\boldsymbol{x}_{\text{true}}, \boldsymbol{b}_0\right)$$

$\mathcal{J}$ is the function of the inversion calculation. $\boldsymbol{b}_0$ and $\Delta \boldsymbol{b}$ are the model parameter vector and its uncertainties, respectively. In the error analysis, the VMR profiles of the climatology based on the UARS/MLS observation were assumed as the true states ($\boldsymbol{x}_{\text{true}}$) for both O_3 and ${}^{18}OOO$. Any undesirable effects inherent in the retrieval algorithm itself were omitted by using $\boldsymbol{x}_{\text{ref}}$ instead of $\boldsymbol{x}_{\text{true}}$ in Eq. (15). The values of $\Delta \boldsymbol{b}$ were estimated as follows. The uncertainties in the air-broadening parameter (γ_{air}) and its temperature dependency (n_{air}) for the O_3 line were estimated to be 3 % and 10 %, respectively, which were typical of errors in past estimations, and that in the line intensity was 1 % (Pickett et al., 1998). For the ${}^{18}OOO$ transition, its spectroscopic parameters' uncertainties were conservatively estimated by multiplying by two for those of the O_3 line considering difficulties in the estimation of the spectroscopic parameters of the

AMTD
6, 8889–8935, 2013

isotopomers and isotopologues. The uncertainty in R_{ANT} and β_{image} was 2 % in FWHM and ±3 dB, respectively, which are same as the error analysis for the V215 ClO by Sato et al. (2012). The uncertainty in the AOS response function was set to 5 % (Mizobuchi et al., 2012).

To estimate the random error we calculated an error due to spectrum statistical noise ($\Delta \boldsymbol{x}_{noise}$), a smoothing error ($\Delta \boldsymbol{x}_{smooth}$) and errors due to uncertainties in the atmospheric temperature and pressure profiles. $\Delta \boldsymbol{x}_{noise}$ was calculated by

$$\Delta \boldsymbol{x}_{noise}[i] = \sqrt{\mathbf{S}_{noise}[i,i]}\,, \tag{16}$$

$$\mathbf{S}_{noise} = \mathbf{D}\mathbf{S}_y\mathbf{D}^{\mathrm{T}}\,,$$

where i in a square bracket indicates the index of a matrix or a vector. $\mathbf{S}_{noise}$ is the covariance matrix for measurement noise. $\mathbf{D}$ is the contribution function matrix. $\Delta \boldsymbol{x}_{smooth}$ was calculated by

$$\Delta \boldsymbol{x}_{smooth}[i] = \sqrt{\mathbf{S}_{smooth}[i,i]} \tag{17}$$

$$\mathbf{S}_{smooth} = (\mathbf{A}-\mathbf{U})\mathbf{S}_z(\mathbf{A}-\mathbf{U})^{\mathrm{T}}\,.$$

$\mathbf{S}_{smooth}$ is the covariance matrix for errors derived from $\mathbf{S}_z$ given by Eq. (6). $\mathbf{A}$ is the averaging kernel matrix. The errors due to uncertainties in the atmospheric temperature and pressure profiles were calculated by Eq. (15) taking into account the vertical correlation between different altitudes (see Eqs. 25–30 in Sato et al., 2012).

Figure 2 shows the reference VMR profiles ($\boldsymbol{x}_{ref}$) and the averaging kernels in the left column. The results of the error analysis for the VMRs of O_3 in window b1 and ^{18}OOO in windows b2 and c1 are shown in the right column. The differences between $\boldsymbol{x}_{ref}$ and $\boldsymbol{x}_{true}$ for all molecules were almost zero, implying that the errors inherent in the algorithm itself were negligibly small. The same retrieval grid was employed for all retrieval windows for obtaining the isotopic ratio without any vertical interpolation in TOROROS, while that of V215 was adjusted to optimize each molecule (see Fig. A1).

AMTD
6, 8889–8935, 2013

The averaging kernel in TOROROS was similar of each other, although the amplitudes were different. The measurement response $\boldsymbol{m}$, that indicates the sensitivity of the observation (see Eq. 19 in Sato et al., 2012), of the b1 O_3 was almost equal to one for all altitudes between 20 and 80 km, thus the retrieved O_3 was less dependent on the a priori VMR. On the other hand, the $\boldsymbol{m}$ of ^{18}OOO in both windows b2 and c1 was larger than 0.9 at altitudes between 28 and 62 km.

The total systematic error of the b1 O_3 was about 2 % from 25 to 65 km. Large contributions were from γ_{air}, the line intensity and the AOS response function. Below 55 km γ_{air} and the line intensity were the dominant causes for the error. The AOS became more important above that altitude. Compared with the errors of the V215 O_3 (see Fig. A1), the errors of the O_3 VMR in TOROROS were considerably decreased, which was not the case for the retrievals of ^{18}OOO. This is because of the different treatment of the tangent height in the VMR retrieval. In the TOROROS algorithm, the tangent height was fixed and the error propagation of γ_{air} was minimized. If the tangent height was retrieved, it was largely dependent on γ_{air}, and this contribution was increased as in V215. The improvement of the AOS response function was also important for reducing the error. The total random error for a single-scan observation was 2–4 % between 25 and 55 km. Errors from the atmospheric pressure profile were the largest below 45 km and those from the temperature profile were the largest above 50 km. $\Delta\boldsymbol{x}_{\mathrm{noise}}$ and $\Delta\boldsymbol{x}_{\mathrm{smooth}}$ were less than 1 % between 25 and 50 km because of the high signal-to-noise ratio of the O_3 transition.

The total systematic error in the ^{18}OOO VMR retrieved in window b2 was 5–15 % and the largest contribution was made by the uncertainty in γ_{air}. The minimum value of the total systematic error was obtained between 40 and 50 km, and the total systematic error increased below and above this altitude region. Similar to O_3, errors from the AOS response function were decreased compared to V215 (see Fig. A1). The total random error was larger than 5 % and increased to 20 % at altitudes above 40 km. Error due to the spectrum noise and smoothing error were more dominant than the errors from the atmospheric temperature and pressure profiles, which is the opposite of the random

AMTD
6, 8889–8935, 2013

error of O_3. The smoothing error dropped off at 57 km. This might be due to the values of $\mathbf{S}_x$ being multiplied by two above 55 km. Both systematic and random errors in the c1 ^{18}OOO were almost the same as the b1 ^{18}OOO, except for errors from γ_{air} around 32 km and from temperature profiles above 45 km.

We estimated the errors of the enrichment by Eq. (14) using the errors of O_3 in window b1 and ^{18}OOO in windows b2 and c1. The systematic and random errors of δ^{18}OOO were calculated respectively, and the results are shown in Fig. 3. The systematic errors using the b2 and c1 ^{18}OOOs were consistent within 2–3 % above 45 km and increased from 6 % (45 km) to more than 10 % (> 60 km). At altitudes between 25 and 40 km δ^{18}OOO using the b2 ^{18}OOO had larger systematic error (14 %) than that of the c1 ^{18}OOO (4–6 %). This is because of the large error due to the uncertainty in γ_{air} of the ^{18}OOO transition in window b2. For δ^{18}OOOs calculated using both windows b2 and c1, errors from ^{18}OOO were dominant rather than O_3. The error from O_3 was about 2–4 % and was decreased compared with that of V215 (see Fig. A2). The random error from the c1 ^{18}OOO was smaller than that from the b2 ^{18}OOO for a single-scan observation. It took the minimum values of 4 % between 30 and 40 km, where the VMRs of O_3 and ^{18}OOO were the maximums, and was increased to more than 15 % below and above this altitude region. Similar to the systematic error, the contribution of errors from ^{18}OOO was larger than that from O_3. The random error was decreased to less than 2 % at altitudes from 25 to 50 km by averaging 100 profiles, which was the case for both windows b2 and c1.

In conclusion, for the error analysis, the largest error source for δ^{18}OOO was the γ_{air} of the ^{18}OOO transition. Indeed, this error source contributed more than 90 % to the total systematic error. We encourage determining γ_{air} of ^{18}OOO transitions at an accuracy of at least the same order of that of the O_3 transition (3 %), although both laboratory experiments and theoretical predictions have large difficulties that must be overcame. Accuracy of spectroscopic parameters, especially γ_{air}, is essential for error in remote-sensing measurements with a high signal-to-noise ratio spectrum (Sato et al., 2012; Sagawa et al., 2013; Kasai et al., 2013).

AMTD
6, 8889–8935, 2013

3.2 Comparison

We compared the VMRs of O_3 and ^{18}OOO derived from SMILES observation by TOROROS and V215. This comparison was performed using an individual profile comparison approach (e.g., Sagawa et al., 2013; Kasai et al., 2013). We selected the data derived from the same scan by TOROROS and V215 under the condition: 20° N–40° N, February–March (2010) and solar zenith angle (SZA) < 80°. The daytime condition was chosen since most of the past measurements compared with SMILES later (see Fig. 6) have been in the daytime. The comparison results in the nighttime are shown in Appendix A2.

In this study we used only the data that satisfied the following requirements for χ^2, measurement response $\boldsymbol{m}$ and VMR value regarding as "good quality". The threshold of χ^2 for O_3 and ^{18}OOO was set to 2.5 and 1.0 for TOROROS, respectively. About 10–20 % data were removed by this χ^2 threshold. The definition of χ^2 is different between the two retrieval algorithms as mentioned in Sect. 2.4. The threshold of χ^2 for the O_3 and ^{18}OOO for V215 was 0.8 and 0.7, respectively as the constraints by the χ^2 threshold were comparable for TOROROS and V215. The requirement of $\boldsymbol{m}$ was $0.9 < \boldsymbol{m} < 1.2$. The VMR threshold was conservatively set to 5 ± 50 ppmv and 20 ± 500 ppbv for O_3 and ^{18}OOO, respectively, to avoid unrealistic VMR values. Data retrieved from L1b data that included any visual field disturbances were also removed. The numbers of profiles of $\delta^{18}OOO$ calculated from the b1 O_3 and the c1 ^{18}OOO with "good quality" were 1145–1377 in an altitude range between 28 and 57 km.

The left panel of Fig. 4 shows the comparison of the O_3 VMRs retrieved by TOROROS (window b1) and by V215 (window B-w1, see Table A1) between 28 and 57 km. The median statistic was used instead of the mean statistic for average state. The VMR of the B-w1 O_3 was linear-interpolated on the retrieval grid of the b1 O_3. The VMR of the b1 O_3 was larger than that of the B-w1 O_3 by at most 0.6 ppmv at altitudes above 32 km. This is desirable, since Kasai et al. (2013) showed that the VMR of the B-w1 O_3 had a negative bias in this altitude region (−0.5 to −1.0 ppmv) due to the problem of the

AMTD
6, 8889–8935, 2013

tangent height determination caused by uncertainty in the non-linearity gain calibration of spectrum brightness temperature.

The comparison for ^{18}OOO is shown in the right side of Fig. 4. The windows B-w4 and C-w5 of V215 correspond to the windows b2 and c1 of TOROROS, respectively. The ^{18}OOOs derived by TOROROS and V215 were in good agreement within the systematic errors for both Bands B and C. Only the b2 ^{18}OOO showed larger VMR than the others at 28 km (represented by dotted line). The difference of ^{18}OOO between Bands B and C in the TOROROS algorithm was within 1 ppbv at altitudes between 32 and 57 km. The usage of common tangent height values in the processing of those two bands largely contributed to reduction of the bias between Bands B and C. In V215, the tangent height values were optimized for each band processing, which resulted in the significant ^{18}OOO difference between Bands B and C.

Figure 5 shows the comparison of δ^{18}OOO between TOROROS and V215. The δ^{18}OOOs of TOROROS were 10–20 % between 32 and 57 km and were smaller than those of V215. This is because of the larger O_3 VMR of window b1 than that in window B-w1 in V215, as shown in Fig. 4. δ^{18}OOO from the b2 ^{18}OOO at 28 km was larger than 30 % because of the large b2 ^{18}OOO VMR. We recommend that data at 28 km not be used. At 57 km, the dispersion of δ^{18}OOO was quite large and we recommend to use the δ^{18}OOO value only for a qualitative discussion, not for a quantitative one. The discrepancies between Bands B and C in the δ^{18}OOO derived by TOROROS were smaller than those of V215, even though there were small differences within 3 % in the δ^{18}OOO of TOROROS above 32 km. The enrichments of TOROROS showed a decrease at altitudes above 45 km, which is discussed in Sect. 4.

The SMILES δ^{18}OOO was compared with the previous measurements in Fig. 6. The δ^{18}OOO from the b1 O_3 and the c1 ^{18}OOO is shown by the blue line. The SMILES δ^{18}OOO increased from 13 % to 18 % as the altitude increased from 32 to 42 km. This was in good agreement with other measurements within the systematic errors in this altitude range. The gradient of the SMILES δ^{18}OOO was about +0.5 % km^{-1}, which was also consistent with the ATMOS observation. Temperature retrieved from

AMTD
6, 8889–8935, 2013

the SMILES observation (window b0) is also shown in Fig. 6 and the SMILES δ^{18}OOO seems to be correlated with the temperature. The correlation between the δ^{18}OOO and the temperature is discussed in Sect. 4.

3.3 Summary of the error of the SMILES δ^{18}OOO

The systematic and random errors in the δ^{18}OOO derived from the SMILES observations are summarized in Table 6. The total systematic error estimated by the error analysis was about 5–15 % at altitudes between 32 and 57 km (see Fig. 3). The dominant source of error was the uncertainty in the γ_{air} of the ^{18}OOO transition for both windows b2 and c1. The total random error was less than 2 % by averaging 100 profiles in this altitude region. The comparison studies showed that the SMILES δ^{18}OOO was in good agreement with the past measurements within the estimated systematic error in the altitude range between 30 to 40 km (see Fig. 6).

4 Discussion

Here we discuss in detail the decreasing δ^{18}OOO with increasing altitude above 45 km derived by TOROROS. As reported by Morton et al. (1990) and Krankowsky et al. (2007), the oxygen isotopic fractionation in the ozone formation (the reaction R1) has the temperature dependence. Figure 7 plots the correlation between δ^{18}OOO and temperature derived from the SMILES observation by TOROROS. δ^{18}OOO was calculated using the VMRs of the b1 O_3 and the c1 ^{18}OOO. The temperature was retrieved in window b0. Only the nighttime data (SZA > 100°) was plotted to remove the photolysis effects. The mean and median δ^{18}OOO values agreed within 1 % excepting 57 km and they can be regarded as representative values between 28 and 52 km. The positive correlation between the δ^{18}OOO and the temperature was clearly obtained that the ozone isotopic enrichment is increased as the temperature increases. This trend is qualitatively consistent with experiments reported by Morton et al. (1990) and Krankowsky

AMTD
6, 8889–8935, 2013

et al. (2007) although their experiments were for the bulk $\delta^{50}O_3$. The gradient of the SMILES $\delta^{18}OOO$ against temperature was roughly estimated to be about 0.25 %/K. The chaperon mechanism, i.e., $ArO + O_2 \rightarrow Ar + O_3$ and $ArO_2 + O \rightarrow Ar + O_3$, should also be considered as an alternative to explain the decreasing $\delta^{18}OOO$ with increasing altitude (Ivanov and Schinke, 2006). Since the decreasing $\delta^{18}OOO$ with increasing altitude was observed in not only the daytime but also the nighttime (see Fig. A4), the photolysis (reaction R2) could not be responsible for the decreasing $\delta^{18}OOO$ with increasing altitude. Ozone isotopic enrichment is assumed to be less dependent on pressure particularly lower than 50 hPa (> 20 km) (e.g., Gao and Marcus, 2002). There have been previous experiments on ozone isotopic enrichment as a function of pressure using O_3 produced by UV photolysis and the discharge of O_2 (Thiemens and Jackson, 1987; Morton et al., 1990). A certain decrement of the enrichment was measured at pressures lower than 8 hPa, however, the authors mentioned it might be due to an apparatus effect caused by the wall effect. Further investigation is suggested to clarify the role that pressure plays on the ozone isotopic enrichment, especially for pressures lower than 1 hPa.

We also investigated whether or not the decreasing $\delta^{18}OOO$ with increasing altitude is caused by errors in the SMILES observations. The error from γ_{air} of the ^{18}OOO transition, which is the largest error source in the total systematic error of $\delta^{18}OOO$, is unlikely to explain the decreasing $\delta^{18}OOO$ with increasing altitude because, firstly, the decreasing $\delta^{18}OOO$ with increasing altitude was observed by two separate observations from frequency Bands B and C (see Fig. 5), secondly, the SMILES $\delta^{18}OOO$ (absolute value and gradient) was in good agreement with the other measurements in the stratosphere. This would not be the case if the γ_{air} value was not realistic. We also discuss the error source that is common for both $\delta^{18}OOO$s from Bands B and C. The systematic error in $\delta^{18}OOO$ due to the uncertainties in O_3 from the frequency window b1 (the largest error source in the retrieval of the O_3 VMR using window b1) was estimated to be less than 4 % (see Fig. 2), which is smaller than the amplitude of the decreasing $\delta^{18}OOO$ with increasing altitude. We also confirmed a priori dependence

AMTD
6, 8889–8935, 2013

of δ^{18}OOO by applying a perturbation of 100 % and obtained almost the same result with difference within 1–2 %. Thus, the error of the SMILES observation considered in this paper could not explain the decreasing δ^{18}OOO with increasing altitude.

We concluded that temperature could be a dominant factor in controlling the vertical profile of δ^{18}OOO in the altitude range of 28 to 52 km.

5 Conclusions

We derived δ^{18}OOO using a retrieval algorithm, named TOROROS, optimized for the oxygen isotopic ratio in ozone in a range between the middle stratosphere and the lower mesosphere from SMILES observations. The TOROROS algorithm is based on the V215 algorithm and includes (i) an a priori covariance matrix constrained by oxygen isotopic ratios in ozone, (ii) an optimization of spectral windows for ozone isotopomers and isotopologues, and (iii) a common tangent height information for all windows. The SMILES δ^{18}OOO was 13 % at 32 km and the systematic error was estimated to be about 5 %. The systematic and random errors were estimated by a quantitative error analysis. The largest error source was an uncertainty in γ_{air} of the ^{18}OOO transition, accounting for more than 90 % of the total systematic error. Determination of γ_{air} of the ^{18}OOO transitions with at least better than 3 % accuracy is desirable for the δ^{18}OOO using the SMILES observation and for other molecules as well.

The SMILES δ^{18}OOO was consistent with those of the past measurements within the estimated systematic errors at altitudes between 30 and 40 km. The vertical profile of δ^{18}OOO obtained in this work showed an increase and a decrease with increasing altitude in the stratosphere and mesosphere, respectively. The peak-height of the δ^{18}OOO value was stratopause and the maximum value of δ^{18}OOO was 18 %. The SMILES δ^{18}OOO had a positive correlation with temperature in the range of 220–255 K. Temperature is probably a dominant factor that controls the vertical profile of δ^{18}OOO in the stratosphere and mesosphere. Since the nighttime δ^{18}OOO also decreased in the lower mesosphere, ozone photolysis might not be a dominant factor for

AMTD
6, 8889–8935, 2013

the decreasing δ^{18}OOO with increasing altitude. To qualify the role of pressure on the ozone isotopic enrichment, especially for pressures lower than 1 hPa, further investigation is recommended.

In this work, we have provided the first observation of δ^{18}OOO over such a wide range as from the stratosphere to the mesosphere. Temperature is probably a dominant factor in controlling the vertical profile of δ^{18}OOO in the altitude range of 28 to 52 km.

Appendix A

Supporting informations

A1 Error analysis for V215

We performed the quantitative error analysis for V215 by the same method as that for the V215 ClO (Sato et al., 2012). Since retrieval procedure of V215 is based on sequentially dependent retrieval steps using the limited spectral windows (see Table A1), we followed the step-by-step retrieval to estimate the errors in the VMR of O_3 and ^{18}OOO, and δ^{18}OOO from the model parameters (Eq. 15). The error from the spectral noise and the smoothing error were calculated by Eqs. (16, 17), respectively.

The window setting of V215 is described as follows. In Band B, first, the tangent height is retrieved using the O_3 line at 625.371 GHz in window B-w0. Window B-w1 is set for the retrieval of the VMR of O_3 with the B-w0 tangent height. The retrieved O_3 VMR and tangent height are used as an a priori in the retrieval of the $H^{35}Cl$ VMR in window B-w2. The VMR of ^{18}OOO is retrieved in window B-w4 using the retrieved parameters in windows B-w0, B-w1 and B-w2 as an a priori. In Band C, the tangent height is retrieved by a bias correction using the ClO line at 649.45 GHz instead of the O_3 line. This tangent height is employed in the retrieval of the VMR of ^{18}OOO in window C-w5.

AMTD
6, 8889–8935, 2013

The error sources in Tables 3–4 were taken into account in this error analysis. The uncertainties in the spectroscopic parameters were the same as the error analysis for TOROROS. As described in Sect. 2.3, the antenna response pattern (R_{ANT}) should be widened, but this procedure was ignored in V215. This was also included in the error sources of V215. The rejection rate of the image band (β_{image}) was assumed to be one in V215, thus, the error due to this assumption was also considered. The uncertainty in the AOS response function was 10 % in the error analysis for V215. The error due to the uncertainty in γ_{air} of the ClO line in Band C was calculated for ^{18}OOO VMR in window C-w5 because the tangent height used in window C-w5 is retrieved using the ClO line as mentioned above. The results of the error analysis for the systematic and random errors in the VMRs of O_3 and ^{18}OOO and the enrichment δ^{18}OOO of V215 are shown in Figs. A1 and A2.

A2 Nighttime comparison between the two retrieval algorithms

The results of the comparison study between the TOROROS and V215 algorithms in the nighttime (SZA > 100°) are shown in Figs. A3–A4 for the VMR of O_3, the VMR of ^{18}OOO and δ^{18}OOO. They showed similar trends as those in the daytime.

A3 Error analysis for temperature retrieved by TOROROS

We estimated the systematic and random errors in the temperature retrieved in window b0 of TOROROS. The method and error sources considered in this analysis were the same as the error analysis for the VMR of O_3 in window b1. The left panel of Fig. A5 shows the reference profile and the averaging kernel for the b0 temperature. The measurement response was larger than 0.9 in the altitude range between 20 and 57 km. The total systematic and random errors in the temperature was about 1–2 % in the stratosphere. The uncertainty in the γ_{air} of the O_3 line contributed more than 90 % of the total systematic error. The AOS response function had larger contribution at altitudes above 50 km. For the random error, the pressure profiles was the dominant

AMTD
6, 8889–8935, 2013

source for all altitudes considered in this study. The temperature profile became more important above 50 km.

Acknowledgements. The JEM/SMILES mission is a joint project of the Japan Aerospace Exploration Agency (JAXA) and the National Institute of Information and Communications Technology (NICT). Data processing and other research tasks in the present study were performed with the NICT Science Cloud at NICT as a collaborative research project. The authors wish to acknowledge K. Kikuchi, S. Ochiai (NICT), M. Shiotani (Kyoto University), M. Suzuki (ISAS/JAXA) and colleagues at JAXA and NICT for managing and supporting the SMILES mission. The authors are grateful to K. A. Walker (Toronto University) and M. Mahani (Tohoku University) for scientific and technical discussion. TOS thanks members in Yoshida Group (Tokyo Institute of Technology). The authors also thank K. Muranaga and T. Haru (Systems Engineering Consultants Co. Ltd.) and J. Möller (Molflow Co. Ltd.) for supporting the data processing of the Level-2 research product. TOS is supported by a Grant in Aid for Research Fellowship for Young Scientists DC1 (No. 23-9766) from the Japan Society for the Promotion of Science, and by the Global COE program "Earth to Earths" of the Ministry of Education, Culture, Sports, and Technology, Japan. YK is supported by the Funding Program for Next Generation World-Leading Researchers (NEXT Program) (No. GR101).

References

Baron, P., Urban, J., Sagawa, H., Möller, J., Murtagh, D. P., Mendrok, J., Dupuy, E., Sato, T. O., Ochiai, S., Suzuki, K., Manabe, T., Nishibori, T., Kikuchi, K., Sato, R., Takayanagi, M., Murayama, Y., Shiotani, M., and Kasai, Y.: The Level 2 research product algorithms for the Superconducting Submillimeter-Wave Limb-Emission Sounder (SMILES), Atmos. Meas. Tech., 4, 2105–2124, doi:10.5194/amt-4-2105-2011, 2011. 8893, 8894, 8897

Drouin, B. J. and Gamache, R. R.: Temperature dependent air-broadened linewidths of ozone rotational transitions, J. Mol. Spectrosc., 251, 194–202, doi:10.1016/j.jms.2008.02.016, 2008. 8896, 8917

Gao, Y. Q. and Marcus, R. A.: Strange and unconventional isotope effects in ozone formation, Science, 293, 259–263, doi:10.1126/science.1058528, 2001. 8891

Gao, Y. Q. and Marcus, R. A.: On the theory of the strange and unconventional isotopic effects in ozone formation, J. Chem. Phys., 116, 137–154, doi:10.1063/1.1415448, 2002. 8908

AMTD
6, 8889–8935, 2013

Hathorn, B. C. and Marcus, R. A.: An intramolecular theory of the mass-independent isotope effect for ozone. I, J. Chem. Phys., 111, 4087–4100, doi:10.1063/1.480267, 1999. 8891

Haverd, V., Toon, G. C., and Griffith, D. W. T.: Evidence for altitude-dependent photolysis-induced ^{18}O isotopic fractionation in stratospheric ozone, Geophys. Res. Lett., 32, L22808, doi:10.1029/2005GL024049, 2005. 8891, 8892, 8920, 8929

Hedin, A. E.: Extension of the MSIS thermosphere model into the middle and lower atmosphere, J. Geophys. Res., 96, 1159–1172, doi:10.1029/90JA02125, 1991. 8897

Irion, F. W., Gunson, M. R., Rinsland, C. P., Yung, Y. L., Abrams, M. C., Chang, A. Y., and Goldman, A.: Heavy ozone enrichments from ATMOS infrared solar spectra, Geophys. Res. Lett., 23, 2377–2380, doi:10.1029/96GL01695, 1996. 8891, 8920, 8929

Ivanov, M. V. and Schinke, R.: Recombination of ozone via the chaperon mechanism, J. Chem. Phys., 124, 104303, doi:10.1063/1.2174013, 2006. 8908

Johnson, D. G., Jucks, K. W., Traub, W. A., and Chance, K. V.: Isotopic composition of stratospheric ozone, J. Geophys. Res., 105, 9025–9031, doi:10.1029/1999JD901167, 2000. 8891, 8920, 8929

Kasai, Y. J., Urban, J., Takahashi, C., Hoshino, S., Takahashi, K., Inatani, J., Shiotani, M., and Masuko, H.: Stratospheric ozone isotope enrichment studied by submillimeter wave heterodyne radiometry: the observation capabilities of SMILES, IEEE T. Geosci. Remote, 44, 676–693, doi:10.1109/TGRS.2005.861754, 2006. 8892

Kasai, Y., Sagawa, H., Kreyling, D., Dupuy, E., Baron, P., Mendrok, J., Suzuki, K., Sato, T. O., Nishibori, T., Mizobuchi, S., Kikuchi, K., Manabe, T., Ozeki, H., Sugita, T., Fujiwara, M., Irimajiri, Y., Walker, K. A., Bernath, P. F., Boone, C., Stiller, G., von Clarmann, T., Orphal, J., Urban, J., Murtagh, D., Llewellyn, E. J., Degenstein, D., Bourassa, A. E., Lloyd, N. D., Froidevaux, L., Birk, M., Wagner, G., Schreier, F., Xu, J., Vogt, P., Trautmann, T., and Yasui, M.: Validation of stratospheric and mesospheric ozone observed by SMILES from International Space Station, Atmos. Meas. Tech., 6, 2311–2338, doi:10.5194/amt-6-2311-2013, 2013. 8892, 8894, 8896, 8899, 8904, 8905

Kikuchi, K., Nishibori, T., Ochiai, S., Ozeki, H., Irimajiri, Y., Kasai, Y., Koike, M., Manabe, T., Mizukoshi, K., Murayama, Y., Nagahama, T., Sano, T., Sato, R., Seta, M., Takahashi, C., Takayanagi, M., Masuko, H., Inatani, J., Suzuki, M., and Shiotani, M.: Overview and early results of the Superconducting Submillimeter-Wave Limb-Emission Sounder (SMILES), J. Geophys. Res. Atmos., 115, D23306, doi:10.1029/2010JD014379, 2010. 8892

AMTD
6, 8889–8935, 2013

Krankowsky, D., Lämmerzahl, P., Mauersberger, K., Janssen, C., Tuzson, B., and Röckmann, T.: Stratospheric ozone isotope fractionations derived from collected samples, J. Geophys. Res. Atmos., 112, D08301, doi:10.1029/2006JD007855, 2007. 8891, 8907, 8920, 8929

Liang, M.-C., Irion, F. W., Weibel, J. D., Miller, C. E., Blake, G. A., and Yung, Y. L.: Isotopic composition of stratospheric ozone, J. Geophys. Res. Atmos., 111, D02302, doi:10.1029/2005JD006342, 2006. 8892, 8929

Lyons, J. R.: Transfer of mass-independent fractionation in ozone to other oxygen-containing radicals in the atmosphere, Geophys. Res. Lett., 28, 3231–3234, doi:10.1029/2000GL012791, 2001. 8891

Marquardt, D. W.: An algorithm for least-squares estimation of nonlinear parameters, J. Soc. Industr. Appl. Math., 11, 431–441, doi:10.1137/0111030, 1963. 8900

Mauersberger, K.: Measurement of heavy ozone in the stratosphere, Geophys. Res. Lett., 8, 935–937, doi:10.1029/GL008i008p00935, 1981. 8891

Mizobuchi, S., Kikuchi, K., Ochiai, S., Nishibori, T., Sano, T., Tamaki, K., and Ozeki, H.: In-orbit measurement of the aos (acousto-optical spectrometer) response using frequency comb signals, IEEE J. Sel. Top. Appl., 5, 977–983, 2012. 8896, 8902

Morton, J., Barnes, J., Schueler, B., and Mauersberger, K.: Laboratory studies of heavy ozone, J. Geophys. Res., 95, 901–907, doi:10.1029/JD095iD01p00901, 1990. 8891, 8907, 8908

Ochiai, S., Kikuchi, K., Nishibori, T., and Manabe, T.: Gain nonlinearity calibration of submillimeter radiometer for JEM/SMILES, J. Sel. Topics Appl. Earth Obs. Remote Sens., 5, 962–969, 2012a. 8893

Ochiai, S., Kikuchi, K., Nishibori, T., Mizobuchi, S., and Manabe, T.: Calibration of superconducting submillimeter-wave limb-emission sounder (SMILES) on the ISS, Proc. SPIE 8527, 8527, 85270Q, doi:10.1117/12.977370, 2012b. 8894

Ochiai, S., Kikuchi, K., Nishibori, T., Manabe, T., Ozeki, H., Mizobuchi, S., and Irimajiri, Y.: Receiver performance of the superconducting submillimeter-wave limb-emission sounder (SMILES) on the international space station, IEEE T. Geosci. Remote, 51, 3791–3801, doi:10.1109/TGRS.2012.2227758, 2013. 8901

Pickett, H. M., Poynter, R. L., Cohen, E. A., Delitsky, M. L., Pearson, J. C., and Müller, H. S. P.: Submillimeter, millimeter and microwave spectral line catalog., J. Quant. Spectrosc. Radiat. Transf., 60, 883–890, doi:10.1016/S0022-4073(98)00091-0, 1998. 8896, 8901, 8917

AMTD
6, 8889–8935, 2013

Rienecker, M. M., Suarez, M. J., Todling, R., Bacmeister, J., Takacs, L., Liu, H.-C., Gu, W., Sienkiewicz, M., Koster, R. D., Gelaro, R., Stajner, I., and Nielsen, J. E.: The GEOS-5 Data Assimilation System–Documentation of Versions 5.0.1, 5.1.0, and 5.2.0., Tech. Rep. NASA/TM-2008-104606, Vol. 27, National Aeronautics and Space Administration, avialable at: http://mls.jpl.nasa.gov/data/datadocs.php (Last access on 8 October 2013), 2008. 8897

Rodgers, C. D.: Inverse methods for atmospheric sounding: theory and practice, series on atmospheric, oceanic and planetary physics, World Sci., 2, 3605–3609, 2000. 8893

Rothman, L. S., Gordon, I. E., Barbe, A., Benner, D. C., Bernath, P. F., Birk, M., Boudon, V., Brown, L. R., Campargue, A., Champion, J.-P., Chance, K., Coudert, L. H., Dana, V., Devi, V. M., Fally, S., Flaud, J.-M., Gamache, R. R., Goldman, A., Jacquemart, D., Kleiner, I., Lacome, N., Lafferty, W. J., Mandin, J.-Y., Massie, S. T., Mikhailenko, S. N., Miller, C. E., Moazzen-Ahmadi, N., Naumenko, O. V., Nikitin, A. V., Orphal, J., Perevalov, V. I., Perrin, A., Predoi-Cross, A., Rinsland, C. P., Rotger, M., Šimečková, M., Smith, M. A. H., Sung, K., Tashkun, S. A., Tennyson, J., Toth, R. A., Vandaele, A. C., and Vander Auwera, J.: The HITRAN 2008 molecular spectroscopic database, J. Quant. Spectrosc. Radiat. Transf., 110, 533–572, doi:10.1016/j.jqsrt.2009.02.013, 2009. 8896, 8917

Sagawa, H., Sato, T. O., Baron, P., Dupuy, E., Livesey, N., Urban, J., von Clarmann, T., de Lange, A., Wetzel, G., Kagawa, A., Murtagh, D., and Kasai, Y.: Comparison of SMILES ClO profiles with other satellite and balloon-based measurements, Atmos. Meas. Tech. Discuss., 6, 613–663, doi:10.5194/amtd-6-613-2013, 2013. 8904, 8905

Sato, T. O., Sagawa, H., Kreyling, D., Manabe, T., Ochiai, S., Kikuchi, K., Baron, P., Mendrok, J., Urban, J., Murtagh, D., Yasui, M., and Kasai, Y.: Strato-mesospheric ClO observations by SMILES: error analysis and diurnal variation, Atmos. Meas. Tech., 5, 2809–2825, doi:10.5194/amt-5-2809-2012, 2012. 8901, 8902, 8903, 8904, 8910

Thiemens, M. H. and Jackson, T.: Production of isotopically heavy ozone by ultraviolet light photolysis of O_2, Geophys. Res. Lett., 14, 624–627, doi:10.1029/GL014i006p00624, 1987. 8908

Worden, J., Bowman, K., Noone, D., Beer, R., Clough, S., Eldering, A., Fisher, B., Goldman, A., Gunson, M., Herman, R., Kulawik, S. S., Lampel, M., Luo, M., Osterman, G., Rinsland, C., Rodgers, C., Sander, S., Shephard, M., and Worden, H.: Tropospheric Emission Spectrometer observations of the tropospheric HDO/H_2O ratio: estimation approach and characterization, J. Geophys. Res. Atmos., 111, D16309, doi:10.1029/2005JD006606, 2006. 8898

AMTD
6, 8889–8935, 2013

Table 1. Spectral windows of TOROROS.

Window/Band	Frequency range	Target	Altitude range
b1/Band B	625.042–625.642 GHz	O_3,	20–80 km
b2/Band B	625.522–625.642 GHz	^{18}OOO, $O_3{}^*$	30–60 km
c1/Band C	649.000–649.350 GHz	^{18}OOO, ^{17}OOO	25–60 km
b0/Band B	625.042–625.642 GHz	Temperature	20–60 km

AMTD
6, 8889–8935, 2013

Table 2. Spectroscopic parameters of transitions of O_3, ^{18}OOO and ^{17}OOO observed in the spectral windows of TOROROS. The values of intensity and γ_{air} are assumed at 300 K. Intensity is represented by a base-10 logarithm. ^{17}OOO has hyperfine structure splittings because of the nuclear spin of ^{17}O. Only the transition that has the largest line intensity in the series of the hyperfine structure splittings is shown. The updated value from V215 is italic.

Species	Window	Frequency [GHz]	Intensity [MHz nm^2]	γ_{air} [MHz Torr^{-1}]	n_{air} [–]	Quantum numbers $N'_{K'_a,K'_c}$	–	$N''_{K''_a,K''_c}$
O_3	b1	625.3712420[a]	−3.8748[b]	*3.06*[c]	*0.81*[c]	$15_{6,10}$	–	$16_{5,11}$
O_3*(v2)	b1/b2	625.6119575[d]	−6.2140[d]	2.72[b]	*0.83*[b]	$38_{9,29}$	–	$39_{8,32}$
^{18}OOO	b1/b2	625.5636585[d]	−3.4532[b]	2.87[e]	0.79[e]	$23_{4,19}$	–	$23_{3,20}$
^{18}OOO	c1	*649.1371670*[d]	−3.4919[b]	2.82[b]	0.79[e]	$26_{4,23}$	–	$26_{3,24}$
^{18}OOO	c1	*649.1386510*[d]	−4.2063[b]	2.67[b]	0.83[e]	$41_{2,39}$	–	$41_{1,40}$
^{18}OOO	c1	*649.1515995*[d]	−4.2237[b]	2.89[b]	0.79[e]	$22_{7,16}$	–	$23_{6,17}$
^{18}OOO	c1	*649.1524085*[d]	−4.2237[b]	2.87[b]	0.68[b]	$22_{7,15}$	–	$23_{6,18}$
^{17}OOO	c1	649.2752349[d]	−4.0646[d]	3.03[e]	0.77[e]	$14_{4,10}$	–	$14_{3,11}$

[a] Private communication with H. Ozeki.
[b] Private communication with the MLS team.
[c] Complex Robert–Bonamy (CRB) calculation performed by Drouin and Gamache (2008).
[d] The JPL catalog (Pickett et al., 1998).
[e] The HITRAN 2008 database (Rothman et al., 2009).

AMTD
6, 8889–8935, 2013

Table 3. Sources of systematic error and their uncertainties considered in the error analysis. Spectral windows that used for the VMR retrieval is shown in the parenthesis.

Error Sources	Uncertainty O_3 (b1)	Uncertainty ^{18}OOO (b2)	Uncertainty ^{18}OOO (c1)	Calculation equation
γ_{air}^{1}	3 %	6 %	6 %	Eq. (15)
n_{air}^{1}	10 %	20 %	20 %	Eq. (15)
Line intensity[1]	1 %	2 %	2 %	Eq. (15)
Antenna beam pattern		2 % in FWHM of R_{ANT}		Eq. (15)
SBS characteristics		±3 dB in β_{image}		Eq. (15)
AOS response function		5 % in FWHM		Eq. (15)
Other source	None	From O_3 line[2]	None	Eq. (15)

[1] Of each observed transition.
[2] Uncertainties in the spectroscopic parameters of the O_3 line at 625.371 GHz.

AMTD
6, 8889–8935, 2013

Table 4. Same as Table 3 but for random error.

Error Sources	Uncertainty O_3 (b1)	Uncertainty ^{18}OOO (b2)	Uncertainty ^{18}OOO (c1)	Calculation equation
Spectrum noise	0.5 K			Eq. (16)
Smoothing error	Same setting as the retrieval processing for each window			Eq. (17)
Temperature profile	3 K (TR), 10 K (ST), 30 K (ME), and 50 K (TH)[1]			Eq. (15)
Pressure profile	3 %			Eq. (15)

[1] TR: troposphere (0–17 km). ST: stratosphere (17–45 km). ME: mesosphere (45–94 km). TH: thermosphere (94–120 km).

AMTD
6, 8889–8935, 2013

Table 5. Summary of information from SMILES and past measurements used in the comparison shown in Fig. 5.

Instrument	Latitude[1]	Month/Year[1]	Altitude	Reference
SMILES (from ISS)	20° N–40° N	Feb–Mar 2010	32–57 km	This paper
Mass spectrometry of collected ozone by balloon	43.7° N	3 Oct 1998, 11 Oct 1999, 4 Oct 2000 11 May 2001, 25 Apr 2002	21–36 km	Krankowsky et al. (2007)
JPL MkIV FTIR spectrometer (balloon-based)	34° N	9 Mar 1993, 14 Feb 1994, 27 Feb 1996	18–41 km	Haverd et al. (2005)
FIRS-2 FT spectrometer (balloon-based)	30° N–35° N, 68° N (in 1997)	26 Sep 1989, 4 Jun 1990, 29 May 1992, 29 Sep 1992, 23 Mar 1993, 22 May 1994 30 Apr 1997	20–40 km	Johnson et al. (2000)
ATMOS FTIR spectrometer (space-based)	80° S–80° N	Apr 1985, Apr 1992 May 1993, Nov 1994	25–41 km	Irion et al. (1996)

[1] Note that the information is only for this comparison not for their whole observations.

AMTD
6, 8889–8935, 2013

Table 6. Summary of the error in δ^{18}OOO derived from the SMILES observation by TOROROS. The numbers in the left and right side are for δ^{18}OOO from the b2 ^{18}OOO and the c1 ^{18}OOO, respectively, for the median value of δ^{18}OOO, SE, RE (1) and RE (100).

Altitude	δ^{18}OOO[1]	SE[2]	RE (1)[3]	RE (100)[4]	VR[5]	Main error source
52 km	15 %/18 %	8 %/7 %	20 %/17 %	2 %/2 %	5 km	γ_{air} of the ^{18}OOO transition
42 km	16 %/20 %	7 %/5 %	8 %/6 %	1 %/1 %	5 km	γ_{air} of the ^{18}OOO transition
32 km	15 %/16 %	14 %/5 %	10 %/5 %	1 %/1 %	5 km	γ_{air} of the ^{18}OOO transition

[1] Median value under the condition of 20° N–40° N, Feb–Mar (2010) and SZA < 80°.
[2] Systematic error.
[3] Random error for a single-scan observation.
[4] Random error in the average of 100 profiles.
[5] Vertical resolution.

AMTD
6, 8889–8935, 2013

Table A1. Spectral windows of V215.

Window/Band	Frequency range	Target	Altitude range	Corresponding window in TOROROS
B-w0/Band B	625.042–625.612 GHz	Tangent height	18–70 km	–
B-w1/Band B	625.042–625.612 GHz	O_3, Temperature	18–100 km	b1
B-w2/Band B	625.714–626.264 GHz	$H^{35}Cl$, $O^{17}OO$	16–100 km	–
B-w4/Band B	625.500–625.830 GHz	^{18}OOO, $O^{17}OO$, HO_2	20–90 km	b2
C-w0/Band C	649.120–650.320 GHz	Tangent height	11–40 km	–
C-w5/Band C	649.000–649.300 GHz	^{18}OOO, ^{17}OOO	25–60 km	c1

AMTD
6, 8889–8935, 2013

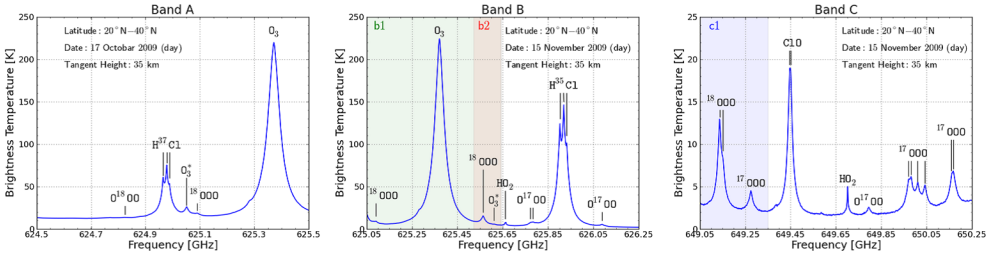

Fig. 1. SMILES observation spectra (Level-1b version 008) of Band A (left), Band B (center) and Band C (right). 50 scans were accumulated under the following conditions. Tangent height: 35 ± 2.5 km. Latitude: 20° N–40° N. Time: Daytime on 17 October (Band A) and 15 November (Bands B and C) in 2009. Shaded area represents the frequency region of the spectral window b1, b2 and c1 by green, red and blue color, respectively (see Table 1).

AMTD
6, 8889–8935, 2013

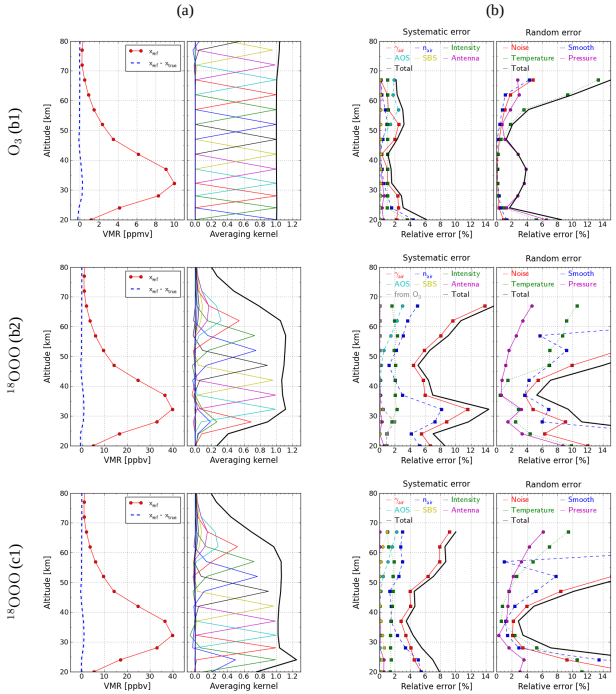

Fig. 2. Reference VMR profiles for the error analysis and the relative errors of O_3 in window b1 (top), ^{18}OOO in window b2 (middle) and ^{18}OOO in window c1 (bottom) retrieved by TOROROS. Column **(a)** shows the reference profile $\boldsymbol{x}_{\mathrm{ref}}$ (red) and the difference between $\boldsymbol{x}_{\mathrm{ref}}$ and the true profile $\boldsymbol{x}_{\mathrm{true}}$ assumed in the error analysis (blue) in the left panel. The measurement response is represented by the black line and the averaging kernel for each altitude is also displayed in the right panel. Column **(b)** shows relative errors for the systematic and random errors in the left and right panels respectively. The random error is for a single-scan observation. The error sources and the estimated uncertainties are listed in Tables 3 and 4.

AMTD
6, 8889–8935, 2013

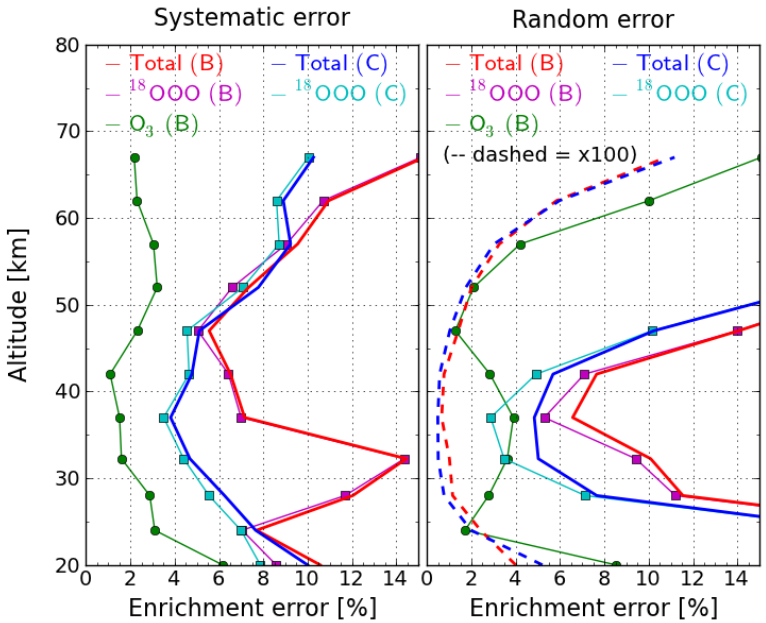

Fig. 3. Errors in the enrichment δ^{18}OOO obtained by TOROROS. Systematic and random errors are shown in the left and right panels, respectively. Random errors are represented by solid and dashed lines for a single-scan observation and the average of 100 profiles, respectively. Total errors in δ^{18}OOO from the ^{18}OOOs in windows b2 and c1 are represented by red and blue lines. The purple, light blue and green lines show the errors in δ^{18}OOO caused by the error sources in the retrievals of ^{18}OOO (window b2), ^{18}OOO (window c1), and O_3 (window b1), respectively.

AMTD
6, 8889–8935, 2013

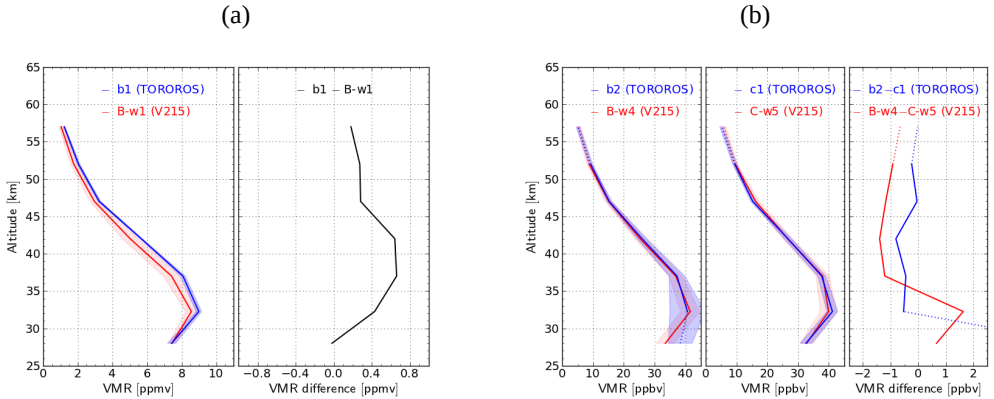

Fig. 4. Comparison between VMRs of O_3 **(a)** and ^{18}OOO **(b)** retrieved by TOROROS (blue) and V215 (red). Latitude: 20° N–40° N. Month: February–March (2010). Solar zenith angle: < 80° (daytime). Only data with "good quality", see text, are used for this comparison. The systematic errors estimated by the error analysis are represented by the shaded area. In column **(a)**, the left and right panels display the median values and their differences, respectively, which is same for column **(b)** but there are two median values of ^{18}OOO VMRs in Bands B and C. The dotted line represents data that the dispersion is quite large or the number of profiles is small, which is same for the figures of the comparison study.

AMTD
6, 8889–8935, 2013

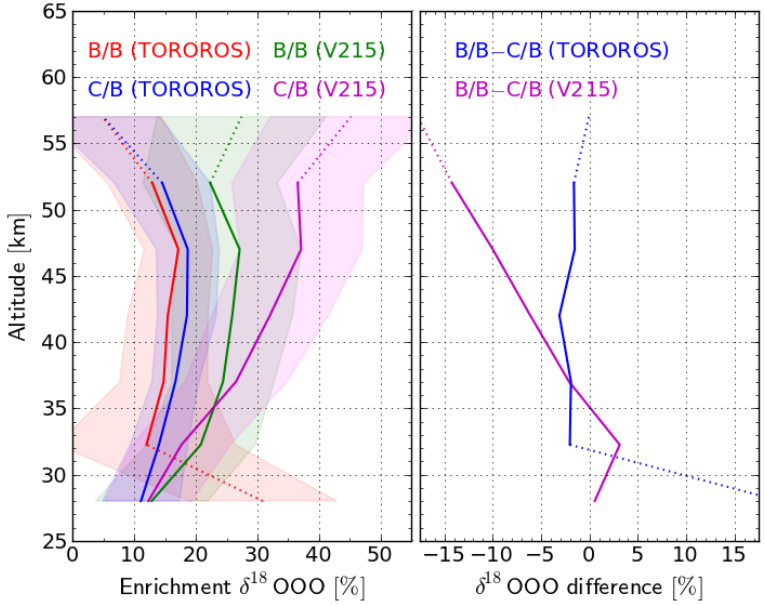

Fig. 5. Comparison of δ^{18}OOO between TOROROS and V215 in Bands B and C. The ranges of latitude, month and SZA was the same as the comparison in Fig. 4. Only data with "good quality" were used in this study. The red and blue line represents the δ^{18}OOO calculated by the ^{18}OOO of Band B (window b2) and Band C (window c1), respectively. The O_3 of Band B (window b1) was common to both ^{18}OOOs. The green and purple line is δ^{18}OOO for the product of V215. The shaded areas represent the systematic errors estimated by the error analyses (see Figs. 3 and A2). The differences between Bands B and C are shown in the right panel by the blue and purple lines for TOROROS and V215, respectively. See the caption of Fig. 4 for the dotted line.

AMTD
6, 8889–8935, 2013

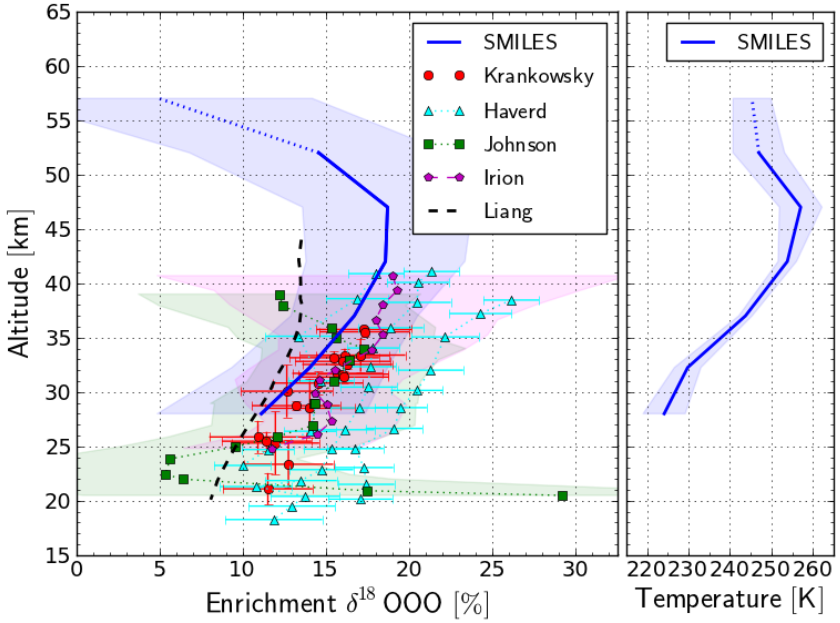

AMTD
6, 8889–8935, 2013

Vertical profile of δ^{18}OOO up to lower mesosphere

T. O. Sato et al.

Fig. 6. Comparison of δ^{18}OOO derived from the SMILES observation by TOROROS with the past measurements. The blue line represents the SMILES δ^{18}OOO obtained from the b1 O_3 and the c1 ^{18}OOO. The data selection is the same as the other comparisons in this paper (Figs. 4 and 5). The estimated systematic error is represented by the shaded area. See the caption of Fig. 4 for the dotted line. The red circle denotes the observations using a mass spectrometer (Krankowsky et al., 2007). The error bar represents the 2−σ standard deviation. These data are multiplied by a factor of 1.196 (= 12.2/10.2) to translate from δ^{18}O (bulk) to δ^{18}OOO. The factor is estimated from the observation by Johnson et al. (2000), whose measurement results are shown by green squares with shaded areas of the estimated precisions. The light blue triangle represents the observations of Haverd et al. (2005). The error bar represents the estimated precision. The ATMOS observation (Irion et al., 1996) is represented by purple marker with shaded area of the 1−σ standard deviation. The black dashed line is the 1–d model simulation of δ^{18}OOO by Liang et al. (2006). Further information on the past measurements is shown in Table 5. Note that the error bars and the shaded areas are used to distinguish between errors in one measurement and in averaged values of several measurements, respectively. The vertical temperature profile retrieved from the SMILES observation is shown (window b0) in the right panel. Shaded area represents the estimated systematic error in the temperature.

AMTD
6, 8889–8935, 2013

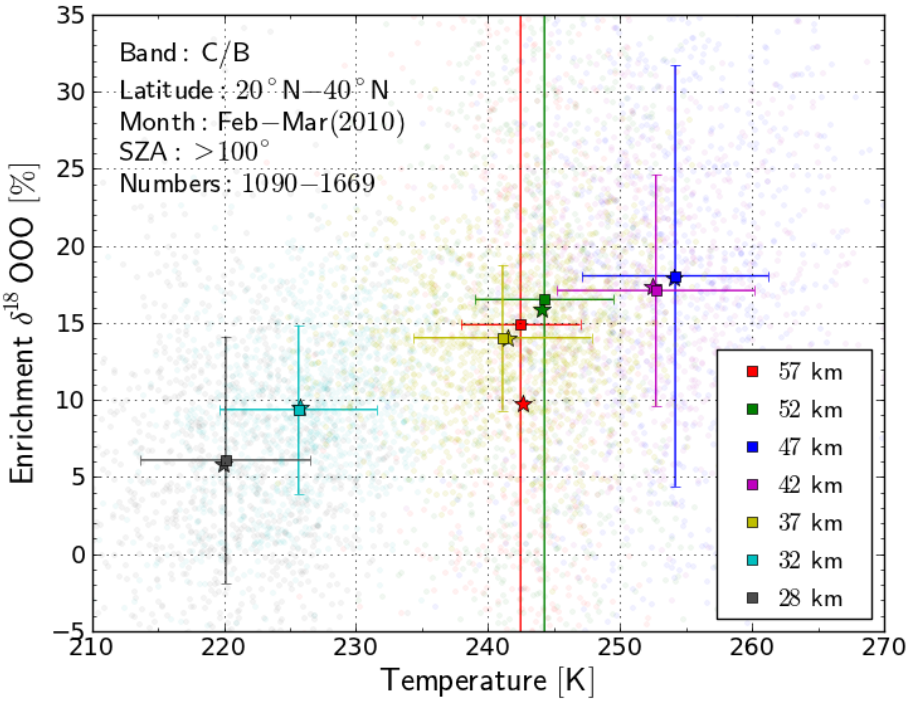

Fig. 7. Correlation between δ^{18}OOO and temperature derived from the SMILES observation. δ^{18}OOO is calculated using the b1 O_3 and c1 ^{18}OOO. The temperature was retrieved in window b0 of TOROROS. Latitude: 20° N–40° N. Month: February–March (2010). Solar zenith angle: > 100° (nighttime). Only data with "good quality", see text, were used. The number of the average for each altitude is shown (the minimum and the maximum values). The mean value for each altitude is plotted by a square marker with an error bar of 1–σ standard deviation. The median value is plotted by a star marker.

AMTD
6, 8889–8935, 2013

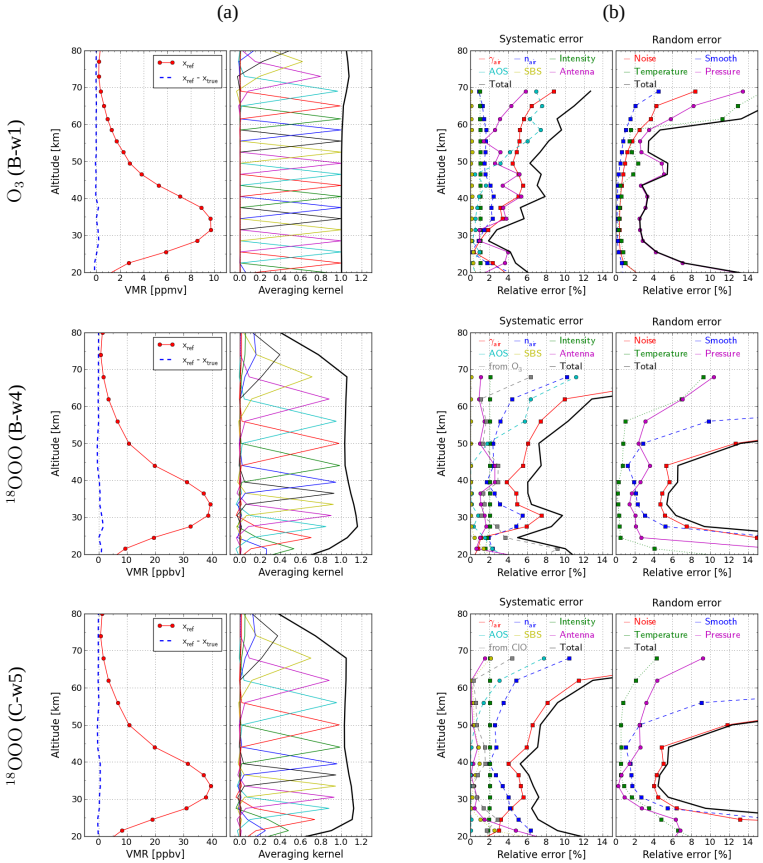

Fig. A1. Same as Fig. 2 but for the O_3 in B-w1 (top), ^{18}OOO in B-w4 (middle) and ^{18}OOO in C-w5 (bottom) of V215.

AMTD
6, 8889–8935, 2013

Vertical profile of $\delta^{18}OOO$ up to lower mesosphere

T. O. Sato et al.

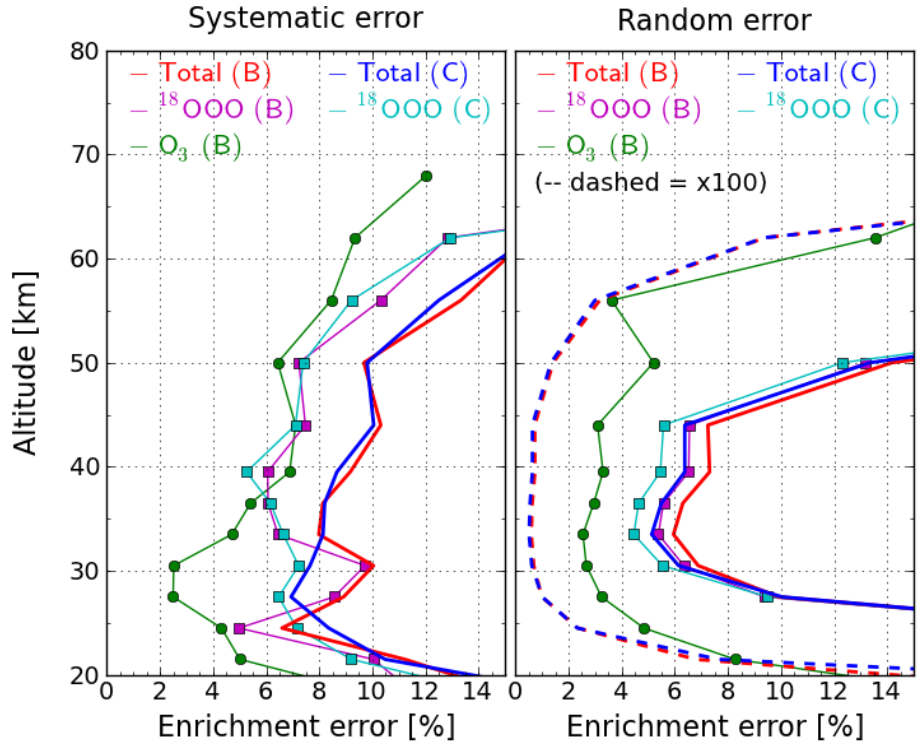

Fig. A2. Same as Fig. 3 but for V215.

AMTD
6, 8889–8935, 2013

Vertical profile of δ^{18}OOO up to lower mesosphere

T. O. Sato et al.

(a) (b)

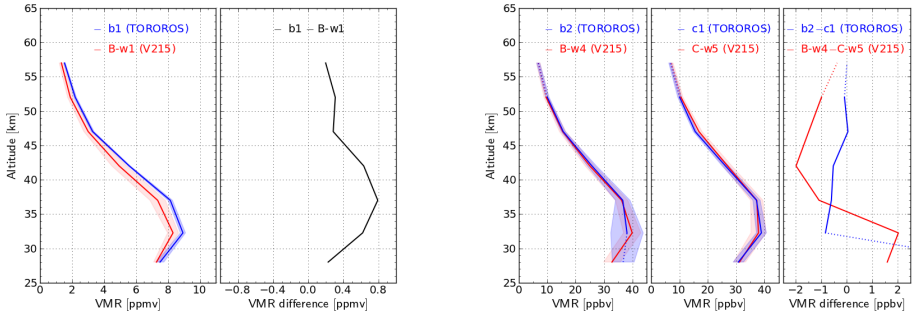

Fig. A3. Same as Fig. 4 but in the nighttime.

AMTD
6, 8889–8935, 2013

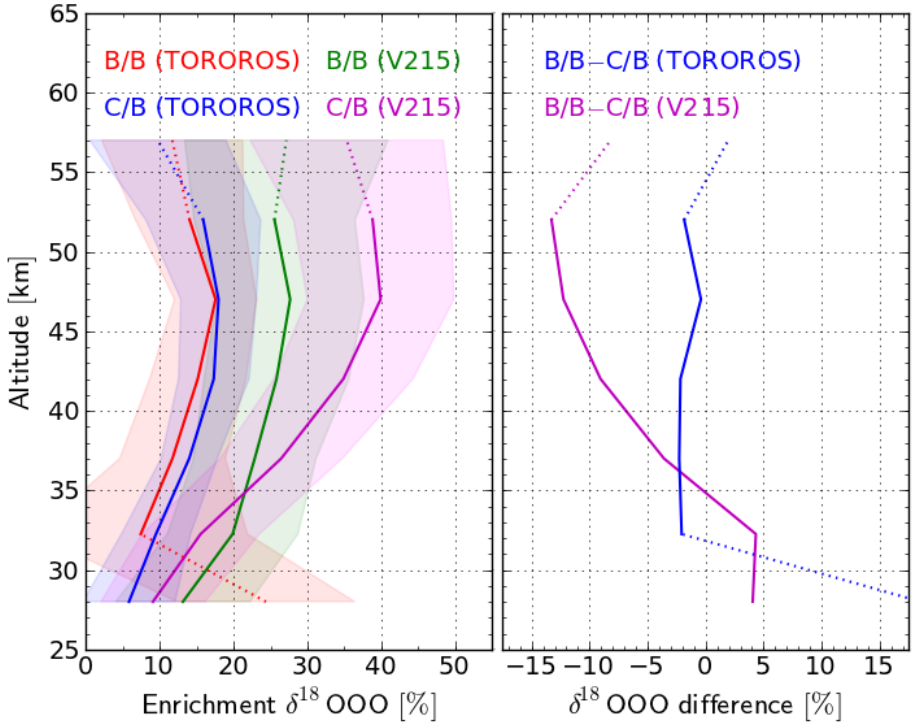

Fig. A4. Same as Fig. 5 but in the nighttime.

AMTD
6, 8889–8935, 2013

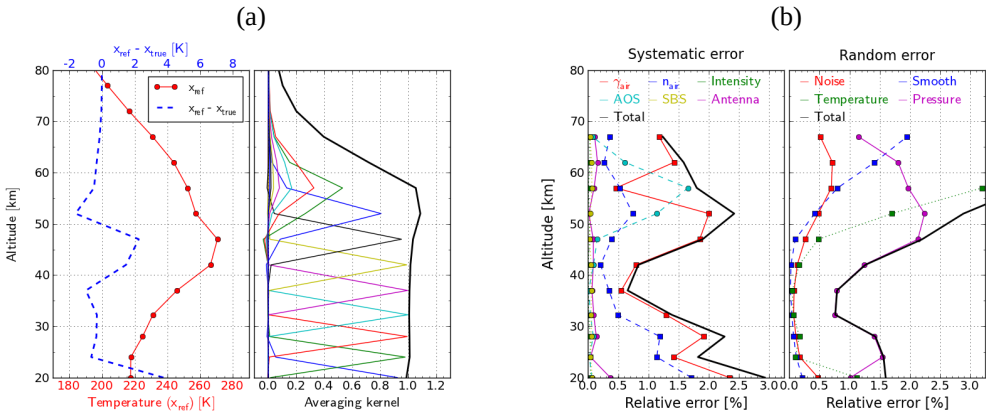

Fig. A5. Same as Fig. 2 but for the temperature retrieved in window b0. In the panel to display the reference temperature profile ($\boldsymbol{x}_{\text{ref}}$), the scale of $\boldsymbol{x}_{\text{ref}}$ and the difference ($\boldsymbol{x}_{\text{ref}} - \boldsymbol{x}_{\text{true}}$) is shown in lower and upper x-axis, respectively.

AMTD
6, 8889–8935, 2013